Physics and Imaging in Radiation Oncology 39 (2026) 100992

Contents lists available at ScienceDirect

Physics and Imaging in Radiation Oncology

journal homepage: www.sciencedirect.com/journal/physics-and-imaging-in-radiation-oncology

Original Research Article

Assessing the quality of deformable image registration in magnetic resonance image guided carbon ion liver radiotherapy with an anthropomorphic phantom

Rita Pestana [a,b,c,*], Anahita Bakhtiari Moghaddam [b,d,e], Friderike K. Longarino [a,b,c,h], Cedric Beyer [a,b,c], Abdallah Qubala [b,c], Katharina Seidensaal [a,b,c], Jürgen Debus [a,b,c,f,g], Sebastian Klüter [a,b], Armin Runz [b,d], Oliver Jäkel [b,c,d], Julia Bauer [i]

[a] Department of Radiation Oncology, Heidelberg University Hospital, Heidelberg, Germany
[b] Heidelberg Institute for Radiation Oncology (HIRO) and National Center for Radiation Research in Oncology (NCRO), Heidelberg, Germany
[c] Heidelberg Ion Beam Therapy Center (HIT), Heidelberg University Hospital, Heidelberg, Germany
[d] Division of Medical Physics in Radiation Oncology, German Cancer Research Center (DKFZ), Heidelberg, Germany
[e] Faculty of Medicine, University of Heidelberg, Germany
[f] National Center for Tumor Diseases (NCT), NCT Heidelberg, a partnership between DKFZ and Heidelberg University Hospital, Heidelberg, Germany
[g] German Cancer Research Center (DKFZ) Heidelberg, Clinical Cooperation Unit Radiation Oncology, Heidelberg, Germany
[h] Clinical Cooperation Unit Translational Radiation Oncology, German Cancer Research Center (DKFZ), Heidelberg, Germany
[i] Charité – Universitätsmedizin Berlin, Corporate Member of Freie Universität Berlin and Humboldt Universität zu Berlin, Department of Radiooncology and Radiotherapy, Augustenburger Platz 1, 13353 Berlin, Germany

ARTICLE INFO

Keywords:
Deformable image registration
MR-guided particle therapy
Online adaptive particle therapy
carbon ion liver SBRT

ABSTRACT

Background and Purpose: Carbon ion radiotherapy (CIRT) for liver patients is usually administrated in four high-dose fractions, requiring high geometrical precision. Work is underway to implement online magnetic resonance (MR)-guided adaptive workflows for this indication. For the generation of a daily computed tomography (dCT), deformable image registration (DIR) can be used. Here, a study on a deformable anthropomorphic abdomen phantom was conducted to assess the accuracy of MR-to-CT DIR.

Materials and Methods: We applied eight different static compressions on the phantom to induce deformations, acquired CT and MR images and performed DIR to generate dCT images for each MR. We assessed the geometric uncertainties of DIR for T1- and T2-weighted MRI sequences by comparing the deformed structures against a manually segmented ground-truth. Furthermore, we assessed the DIR impact on the dose distribution on a single-beam CIRT plan, comparing the beam's range (R80%) on the dCT against those of the CT images.

Results: From the geometric analysis, we obtained mean Dice similarity coefficients (DSC) for the liver of 0.94 ± 0.02 for the T1- and 0.95 ± 0.10 for the T2-weighted MR sequences. These values were above the mean deformation induced on the liver (DSC of 0.87 ± 0.08). As for the range uncertainty induced by DIR, we observed mean R80% uncertainties up to 1.35 mm when comparing treatment doses on the dCT and CT images.

Conclusions: Geometric and beam range uncertainties have been assessed systematically and were found to be small. These results support further implementation of an MR-guided DIR-based online adaptive workflow for liver CIRT.

1. Introduction

Carbon ion radiotherapy (CIRT) is a highly effective treatment option for hepatocellular carcinoma (HCC) patients [1–5]. The therapeutic dose is typically prescribed in four high-dose fractions, requiring high geometrical precision [2]. Furthermore, CIRT treatment plans are highly sensitive to anatomical changes along the beam path, due to the steep dose fall-off behind the Bragg peak and the dependence of the range of a charged particle on the stopping power ratio (SPR) [6,7].

Image guidance in proton and carbon ion therapy increasingly relies

* Corresponding author at: Department of Radiation Oncology, Heidelberg University Hospital, Heidelberg, Germany.
E-mail address: Rita.NetoPestana@med.uni-heidelberg.de (R. Pestana).

https://doi.org/10.1016/j.phro.2026.100992
Received 6 November 2025; Received in revised form 24 April 2026; Accepted 6 May 2026
Available online 10 May 2026

on advanced volumetric imaging techniques such as in-room computed tomography (CT) and cone-beam CT (CBCT). This enables precise patient setup verification, anatomical change monitoring, and adaptive treatment strategies to improve targeting accuracy and reduce uncertainties [8,9]. Efforts are being made to implement shuttle-based online magnetic resonance imaging (MRI)-guided adaptive workflows for this indication, aiming at better imaging of the tumour and ensuring the daily coverage of the target volume [10]. For the generation of a daily deformed CT (dCT), deformable image registration (DIR) is used, which maps the corresponding daily structures with the vector field (VF) onto the dCT. As the goal was to clinically implement the workflow on the treatment planning system currently in use, DIR was performed with the ANAtomically CONstrained Deformation Algorithm (ANACONDA).

A complete study of the dCT quality requires the availability of a ground-truth daily CT, containing the same anatomical information as the MRI. This is hard to achieve with patient measurements, as some organs move between the acquisition of both images. In the absence of a ground-truth, a previous study has assessed the accuracy of ANACONDA against other algorithms [11]. For conventional radiotherapy with photons, MRI-guided workflows for HCC have been assessed and implemented [12–14] and the accuracy of MRI-to-CT DIR has been assessed for several algorithms [15]. However, no DIR accuracy studies have been performed for liver MRI-guided CIRT with ANACONDA.

To overcome this limitation and assess the absolute MRI-to-CT DIR quality achieved with ANACONDA, a study using an anthropomorphic phantom known as the Breathing Radiotherapy Visual monitoring, Imaging, and Dosimetric Anthropomorphic (BRaVIDA) [16] was designed and conducted. Geometric and dosimetric uncertainties, which are essential to know in an MRI-guided particle therapy workflow, were fully evaluated.

2. Materials and Methods

2.1. Phantom

The phantom used in this study was BRaVIDA. As depicted in Fig. 1, it is an anthropomorphic phantom containing anatomically realistic models of major abdominal organs, including the liver, kidneys, spleen, stomach, pancreas, intestines, and vertebrae. The organ models exhibit CT numbers and MRI relaxation times comparable to patient tissue [17]. The outer shell, made of Acrylonitrile Butadiene Styrene (ABS), lacks MRI contrast. Two stamps were placed at the diaphragm and lower membranes enabling respiratory motion simulation using an in-house hydraulic system developed at the German Cancer Research Center (DKFZ).

2.2. Image acquisition

For the image acquisition, the upper stamp was moved between the scans in order to induce deformations of the organs, in particular, the liver. Static MR and CT images were acquired at different stamp positions: 0 mm with no compression (further referred to as reference position), and 5–40 mm in 5 mm increments. All of the measurements were carried out on the same day to minimize setup uncertainties. While the MRI measurements took place in the morning, the CT images were acquired in the afternoon. The hydraulic system had to be detached before and after the MRI measurements to keep the motors outside of the room due to the magnetic field. The hydraulic system was refilled before the image modality was changed to compensate for possible oil losses.

Planning CT images were acquired with a SOMATOM Confidence CT scanner (Siemens Healthineers, Forchheim, Germany) with a resolution of $0.98 \times 0.98 \times 3$ mm^3, using the local clinical protocol for liver treatment planning. The MRI images were acquired on a diagnostic device (MAGNETOM Sola MRI scanner (Siemens Healthineers, Forchheim, Germany), $B_0 = 1.5$ T) installed at the Heidelberg Ion Beam Therapy Center (HIT). The MR imaging protocol contained two different sequences: a T2-weighted three-dimensional (3D) turbo spin echo (TSE) sequence with variable flip angle evolution (SPACE) and a T1 3D gradient echo sequences (GRE) with the two-point Dixon technique opposed-phase sequence (T1-Opp). The T2 sequence featured an echo time (TE) of 134 ms and a repetition time (TR) of 1400 ms, while the T1 sequences had TE values of 2.33 ms (in-phase) and 4.39 ms (opposed-phase), with a TR of 6.8 ms. All sequences were sampled with a resolution of $1 \times 1 \times 3$ mm^3 with 3D distortion correction applied.

2.3. Image registration

Image registration was performed in a research version of RayStation® (RaySearch Laboratories, Stockholm, Sweden) 11B. The CT with no compression (both stamps positioned at 0 mm) was used as the reference CT image, and a DIR was performed between this reference CT and the eight MRI images acquired with different upper stamp positions. First, an automatic rigid registration based on grey level information was performed to align the CT and MRI images. Second, a DIR was carried out with ANACONDA [18], the algorithm incorporated in the treatment planning system RayStation 11B, using mutual information as the similarity measure. A detailed description of the parameters used for the DIR is provided in Table S1. With the VF from the DIR, the different dCT images were created and the structures contoured on the reference CT were deformed.

2.4. Geometric evaluation of DIR

To assess the similarity between two organs, the Dice similarity coefficients (DSC) [19] and mean distances to agreement (MDA) [20] were calculated, after rigid registration, using a built-in function in RayStation. For the different scenarios, the following structures were considered: liver, stomach, pancreas, left kidney, right kidney, bowel and spleen.

In the first step, the structures mentioned above were manually contoured by the same observer on all the acquired CT and MRI images. Based on these structures, several aspects have been addressed. The full analysis procedure is summarized in Fig. 2. The DSC and MDA between each CT and MRI acquired with the same compression were calculated to quantify the setup uncertainties between the two imaging modalities (green arrow in Fig. 2). Then, the DSC and MDA values were calculated between the reference MRI and each measurement with a different compression from the same imaging modality, to quantify the deformation induced on the phantom by moving the upper stamp (blue arrow). Finally, the DSC and MDA between the structures on each dCT (mapped with the VF) and those on the corresponding measured CT (manually contoured) were calculated to quantify the geometric uncertainties of DIR (yellow arrow).

2.5. Evaluation of DIR on the dose distribution

For the assessment of the uncertainties of DIR on the dose distribution, a spherical structure with a 2.5 cm diameter was drawn as the planning target volume (PTV) on the reference CT, located in the lower part of the right lobe of the liver. A single-beam CIRT treatment plan with an active raster-scanning technique, according to our institutional protocol, was designed to cover the PTV with a typical liver SBRT prescription for HCC: 4 x 10.5 relative biological effectiveness (RBE)-weighted dose (Gy (RBE)[1]) (see Fig. 3). For the RBE-weighted dose calculations, the local effect model version 1 (LEM I) was used. The targets were then mapped onto the other CT images using a liver-based DIR performed with ANACONDA, using the parameters given in Table S1.

The treatment plan was forward-calculated, without adaptation, on

[1] This nomenclature refers to the ICRU93 definition.

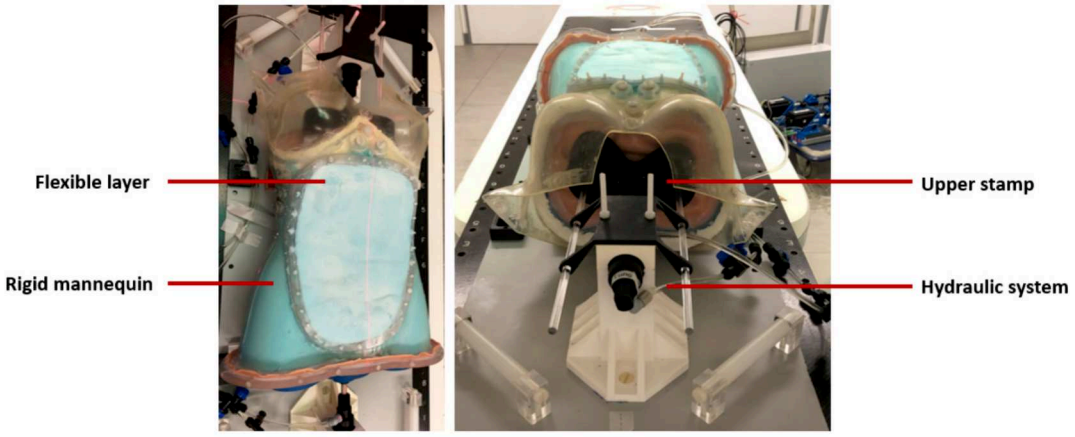

Fig. 1. BRaVIDA, the abdomen phantom used for the measurements is shown. Several parts of the phantom are highlighted: flexible abdomen layer and rigid mannequin (left); upper stamp and hydraulic system (right).

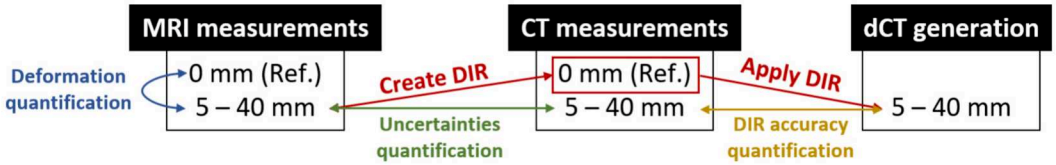

Fig. 2. Schematic representation of the measurements and geometric analysis performed on the imaging data.

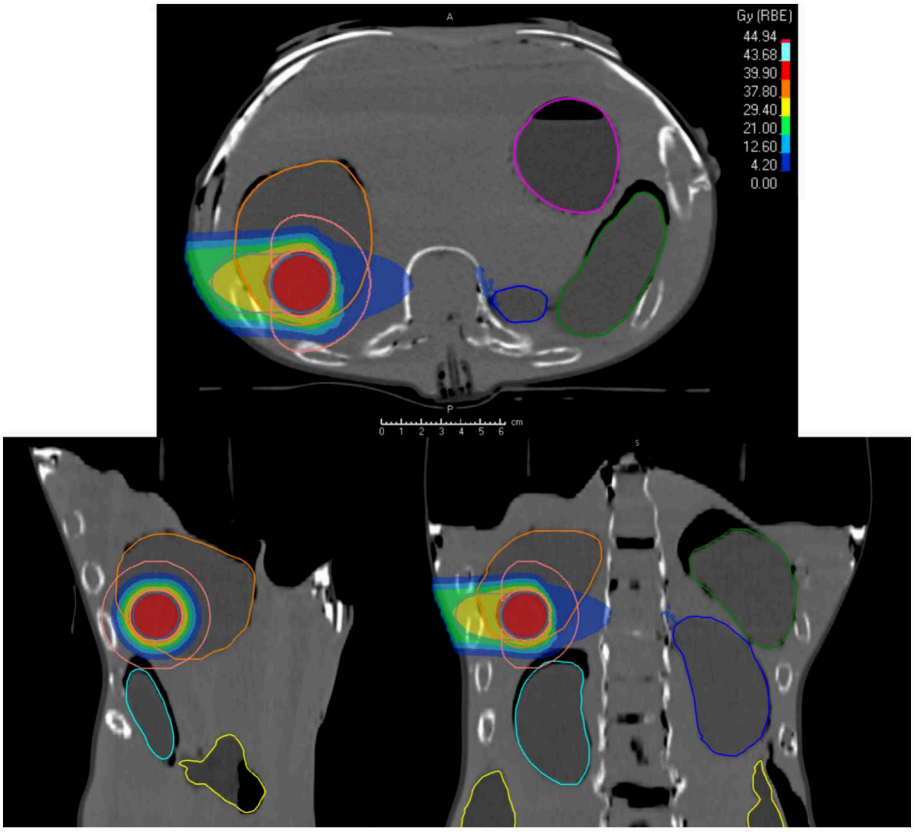

Fig. 3. Target location and respective 4 x 10.5 Gy (RBE) CIRT treatment plan (RBE-weighted), designed on the reference CT image. An axial slice is shown in the top. Sagittal (left) and coronal (right) slices are shown in the bottom where the following organs have been contoured: liver (orange), stomach (magenta), spleen (green), right kidney (cyan), left kidney (blue) and bowel (yellow). (For interpretation of the references to colour in this figure legend, the reader is referred to the web version of this article.)

the different CT and dCT images in RayStation. Since the outer layer of BRaVIDA has no MRI contrast, a region of interest (ROI) with a thickness

of 3 mm and material overwrite with water (mass density = 1.00 g/cm^3) was created on the dCT images to compensate for the absence of this material. A ray-casting algorithm [21] was implemented in Python to cast dose cubes within the scripting environment of RayStation. The dose cubes obtained from the treatment plan forward calculation on the different dCT images were used to generate the 80% distal fall-off (R80%) maps. These maps were then used to detect dose fall-off differences between the dCT and the measured CT images.

3. Results

Fig. 4 shows an example of CT and MRI images of the phantom with the manually contoured structures, along with the corresponding dCT generated using ANACONDA for the T1 and T2 sequences, including the VF structures.

For setup uncertainties, as shown in Fig. 5(b), the mean DSC and corresponding MDA values obtained for the liver were 0.97 ± 0.02 (MDA of 0.90 ± 0.59 mm). Regarding the deformation induced on the liver by moving the upper stamp (see Fig. 5(a)), the mean DSC and MDA for the liver was 0.87 ± 0.08 (3.48 ± 2.36 mm), with MDA values reaching up to 8.17 mm.

For the geometric accuracy of DIR, the DSC values obtained for the T1 sequence (see Fig. 5(c)) ranged between 0.86 (pancreas with 15 mm compression) and 0.97 (liver with 20 mm compression). For the same sequence, MDA values were between 0.59 mm (spleen with 20 mm compression) and 2.0 mm (liver with 30 mm compression). The mean DSC (MDA) for the liver was 0.94 ± 0.92 (1.64 ± 0.45 mm).

For the T2 sequence, as presented in Fig. 5(d), a minimum DSC of 0.83 was obtained for the bowel with a 30 mm compression, while the maximum of 0.96 was achieved for the liver with the stamp at 10 mm. MDA values ranged from 0.8 mm (pancreas with 10 mm compression) and 3.0 mm (stomach with 30 mm compression). Detailed data for all organs is provided in the Supplementary Tables S2–S9.

Fig. 6 depicts the results of the impact of DIR on the dose distribution, showing an illustrative example of the R80% maps obtained from the CT and dCT images, along with the corresponding R80% difference map and histogram calculated on the PTV.

The mean R80% differences between the CT and dCT images for the various upper stamp positions are also presented. These mean differences ranged from 0.04 mm (T2 sequence with 5 mm and with 10 mm compression) to 1.35 mm (T1 sequence with 40 mm compression). Comprehensive tables with the average and standard deviation values for each case are provided in Table S10.

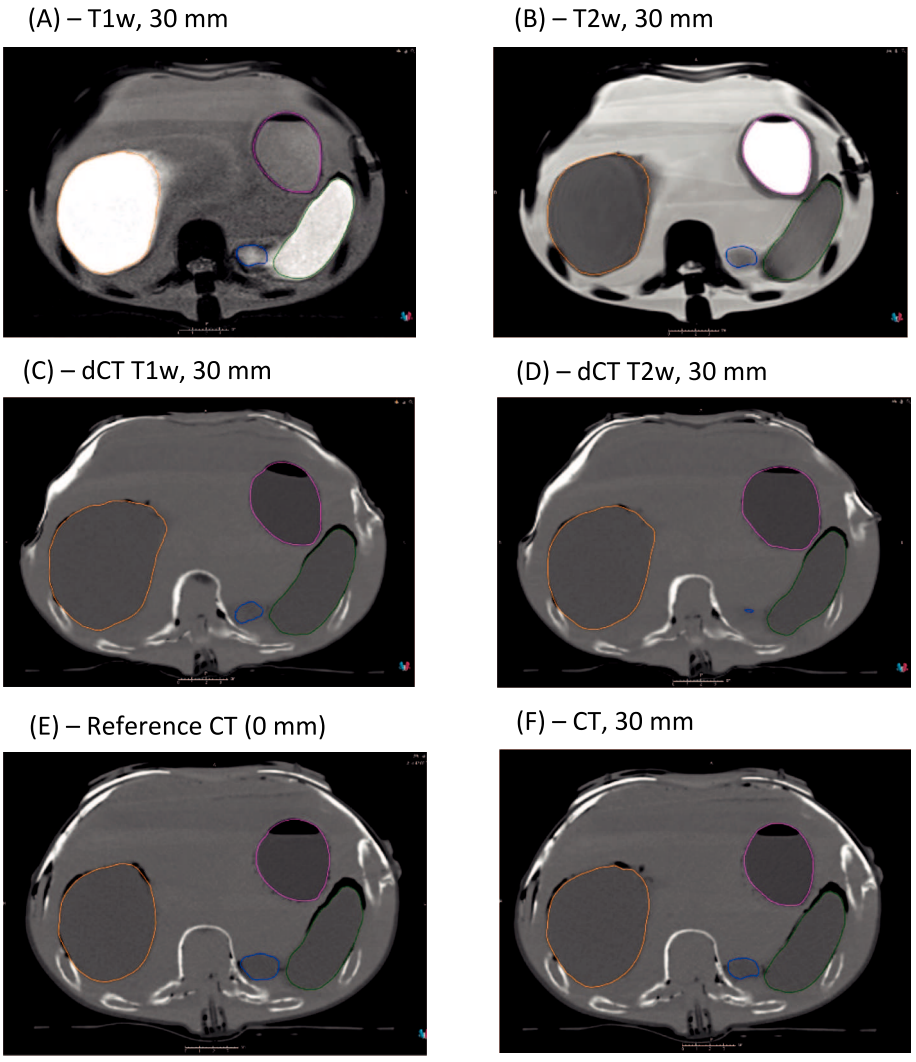

Fig. 4. Illustrative examples of the axial images obtained for the stamp position of 30 mm are shown: T1- (A) and T2-weighted MRI sequences (B), and the corresponding dCT (C) and (D), respectively. In (E), the reference CT is presented, and (F) shows the ground-truth CT measured for the position 30 mm. The following structures are shown: liver (orange), stomach (pink), spleen (green) and left kidney (blue). (For interpretation of the references to colour in this figure legend, the reader is referred to the web version of this article.)

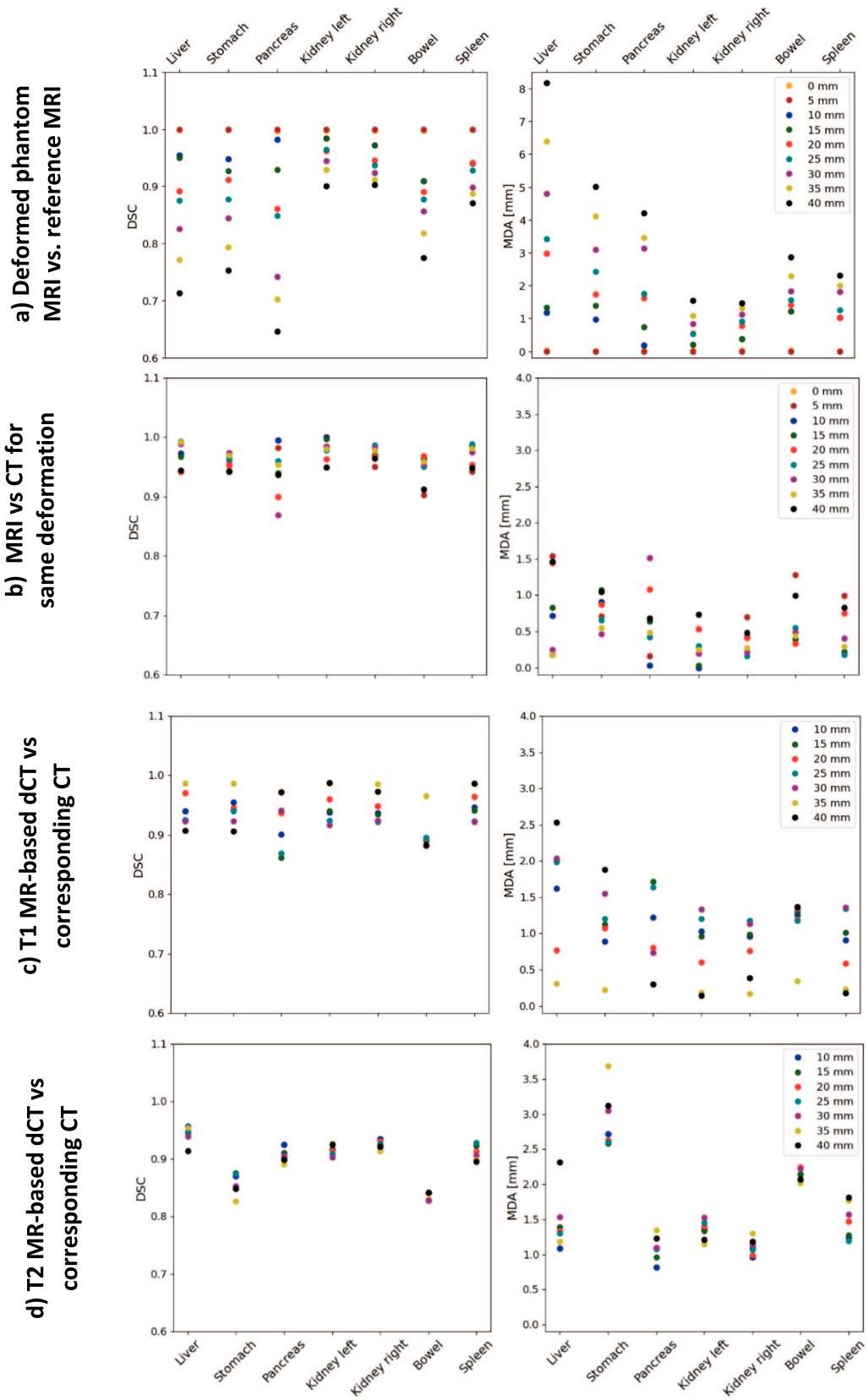

Fig. 5. DSC and MDA obtained from the following comparisons: a) each MRI (with up to 40 mm compression) against the reference MRI (no compression); b) MRI against CT measurements; c) each dCT generated with the T1-weighted sequence against the corresponding CT; d) each dCT generated with the T2-weighted against the corresponding CT.

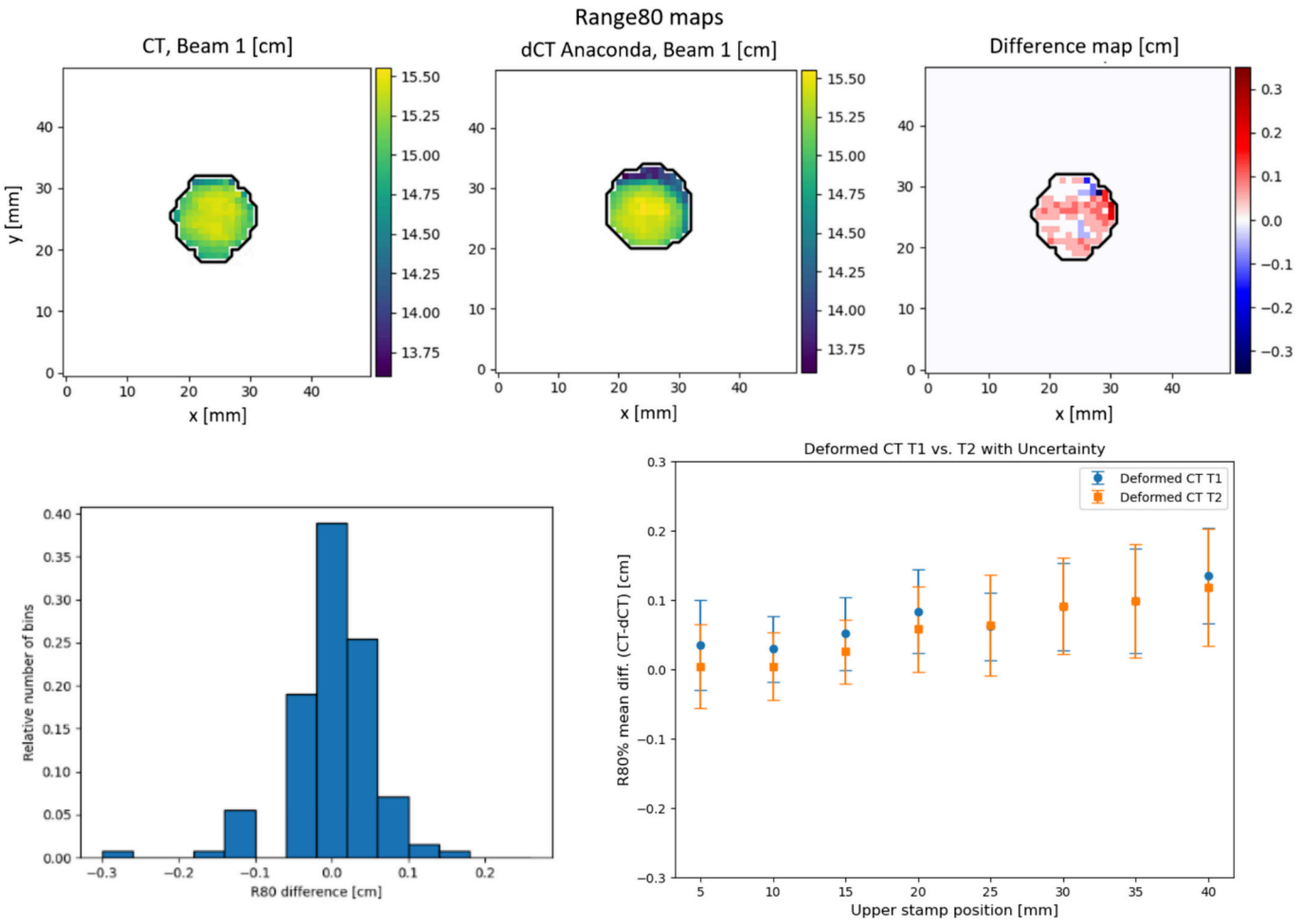

Fig. 6. At the top, an illustrative example of the R80% maps obtained on the projection of the PTV in beam's eye view (black structure) for the CT and dCT images with the upper stamp positioned at 5 mm is shown. At the bottom, the difference map and the respective histogram are shown, as well as the mean differences obtained between the CT and dCT images for the various upper stamp positions, along with their standard deviations, are reported.

4. Discussion

In this study, the accuracy of DIR within a daily MR-guided CIRT workflow for liver SBRT patients was assessed. As part of this evaluation, the geometric accuracy of DIR in mapping the daily MRI contours was quantified. Subsequently, the impact of the resulting dCT on the dose distribution was assessed using a representative single-beam CIRT plan, which is typically used for this clinical indication.

From the geometric assessment of this study, we verified that the deformation induced on the phantom (Fig. 5(b)) is larger than the setup uncertainties, quantified by the comparison of the contours of each MRI against the corresponding CT (Fig. 5(a)). In particular, the maximum MDA obtained for the setup uncertainties on the liver was 1.5 mm, lower than the mean deformation induced on this organ, 3.48 ± 2.36 mm. The deformation on the liver led to MDA values between 1.54 mm and 8.17 mm. These values are consistent with the interfractional liver motion observed in patients, as recently assessed internally at HIT. In a retrospective analysis of six HCC patients, the average MDA between daily CT images and the corresponding planning CT was found to be 3.47 mm ± 1.12 mm, with values ranging from 1.71 mm to 6.12 mm.

The geometric uncertainties of the dCT images generated from the T1- and T2-weighted MRI images, as shown in Fig. 5(c) and (d), respectively, were found to be lower than the deformation induced in the phantom for compressions of 20 mm or greater. For the liver, mean DSC of 0.94 ± 0.02 and 0.95 ± 0.01 were obtained for the T1- and T2-weighted sequences, respectively. These results indicate that the geometric error introduced by adaptation (i.e., through the use of dCT) is smaller than the error resulting from non-adaptation. Moreover, the reported values agree with previous studies using alternative algorithms. For instance, a diffeomorphic transform-based method for MRI-to-CT DIR of the abdomen, proposed by Lei et al. [15], achieved liver DSC values of 0.90 ± 0.04.

Regarding the impact of DIR on the dose distribution, mean R80% deviations of up to 1.35 mm were observed when the dCT images generated from T1- and T2-weighted MRI images were compared to the corresponding measured CT images. It should be noted that the manual definition of the outer layer, which lacks MRI contrast, may introduce additional uncertainty in the range of the carbon ion beam. The average water equivalent path length of the treatment beam is 6.74 cm, so a standard 2.5% CT-to-dose calibration uncertainty [6,22] would lead to a margin of 1.7 mm. Additionally, the beam delivery uncertainty at HIT has been internally estimated at 0.5 mm. When these uncertainties are combined with the geometric uncertainty introduced by our DIR, a total margin of 3.55 mm is obtained. This value remains smaller than the clinically applied isotropic expansion of 5 mm (7 mm in the beam direction) used at HIT for this treatment indication [4].

The presented work is a phantom study and therefore has limitations. Though an anthropomorphic phantom was used, a patient liver might move and behave differently. Furthermore, the mannequin forming the lateral side of the phantom is rigid and therefore did not undergo any deformation. Additional limitations of the study include the uncertainties caused by transporting the phantom between the MRI and CT

scanners and the reproducibility of the different phantom states. For that reason, the differences between each CT and the corresponding MRI were evaluated. Moreover, contouring uncertainties contributed to the overall variability, although all the images were contoured by a single observer. In particular, the T1-weighted MRI images had black boundary artefacts around some organs, making it difficult to accurately contour them.

A retrospective study on a patient cohort treated at HIT is currently underway. Furthermore, a patient shuttle is being integrated in the clinical workflow at HIT [23], allowing patient transfer between the treatment room, CT and MRI scanners in the treatment position. This will enable the generation of a valuable dataset, with ground-truth CT images for the assessment of the outcomes and uncertainties of the adaptive workflow.

In conclusion, an adaptive workflow based on MRI-to-CT and DIR was shown to provide a more accurate representation of daily anatomy than a non-adaptive approach. This improved anatomical accuracy could enable treatment planning margins to be reduced, thereby improving the preservation of healthy liver tissue.

CRediT authorship contribution statement

Rita Pestana: Writing – review & editing, Visualization, Validation, Software, Methodology, Investigation, Formal analysis, Data curation, Conceptualization. **Anahita Bakhtiari Moghaddam:** Writing – review & editing, Resources, Methodology, Investigation, Data curation. **Friderike K. Longarino:** Writing – review & editing, Validation, Methodology, Investigation, Data curation. **Cedric Beyer:** Writing – review & editing, Validation, Software, Investigation, Data curation. **Abdallah Qubala:** Writing – review & editing, Investigation, Data curation. **Katharina Seidensaal:** Writing – review & editing, Validation, Project administration, Methodology, Data curation, Conceptualization. **Jürgen Debus:** Writing – review & editing, Resources, Funding acquisition. **Sebastian Klüter:** Writing – review & editing, Resources, Project administration, Funding acquisition. **Armin Runz:** Writing – review & editing, Validation, Supervision, Resources, Investigation, Funding acquisition. **Oliver Jäkel:** Writing – review & editing, Supervision, Resources, Funding acquisition. **Julia Bauer:** Writing – review & editing, Validation, Supervision, Project administration, Methodology, Funding acquisition, Data curation, Conceptualization.

Declaration of competing interest

The authors declare the following financial interests/personal relationships which may be considered as potential competing interests: Juergen Debus reports a relationship with RaySearch Laboratories AB that includes: funding grants. Juergen Debus reports a relationship with Vision RT Ltd that includes: funding grants. Juergen Debus reports a relationship with Merck Serono GmbH that includes: funding grants. Juergen Debus reports a relationship with Siemens Healthcare GmbH that includes: funding grants. Juergen Debus reports a relationship with PTW-Freiburg Dr. Pychlau GmbH that includes: funding grants. Juergen Debus reports a relationship with Accuray Inc that includes: funding grants. Juergen Debus reports a relationship with Intra OP that includes: non-financial support. Sebastian Klüter has received speaker fees from Siemens Healthineers. The other authors declare that they have no known competing financial interests or personal relationships that could have appeared to influence the work reported in this paper.

Acknowledgements

We thank Alexander Neuholz, Beata Koczur and Thomas Tessonnier for their technical assistance. This work was kindly funded by the German Federal Ministry of Research, Technology and Space within the funding program “Bildgeführte Diagnostik und Therapie – Neue Wege in der Intervention” (ARTEMIS, 13GW0436A). For the publication fee we acknowledge financial support by Heidelberg University.

Appendix A. Supplementary data

Supplementary data to this article can be found online at https://doi.org/10.1016/j.phro.2026.100992.

References

[1] Gkika E, Schultheiss M, Bettinger D, Maruschke L, Neeff HP, Schulenburg M, et al. Excellent local control and tolerance profile after stereotactic body radiotherapy of advanced hepatocellular carcinoma. Radiat Oncol 2017;12:116. https://doi.org/10.1186/s13014-017-0851-7.
[2] Hoegen-Saßmannshausen P, Naumann P, Hoffmeister-Wittmann P, Ben Harrabi S, Seidensaal K, Weykamp F, et al. Carbon ion radiotherapy of hepatocellular carcinoma provides excellent local control: the prospective phase I PROMETHEUS trial. JHEP Rep 2024;6:101063. https://doi.org/10.1016/j.jhepr.2024.101063.
[3] Kim TH, Koh YH, Kim BH, Kim MJ, Lee JH, Park B, et al. Proton beam radiotherapy vs. radiofrequency ablation for recurrent hepatocellular carcinoma: a randomized phase III trial. J Hepatol 2021;74:603–12. https://doi.org/10.1016/j.jhep.2020.09.026.
[4] Hoffmeister-Wittmann P, Hoegen-Saßmannshausen P, Wicklein L, Weykamp F, Seidensaal K, Springfeld C, et al. Stereotactic body radiotherapy with carbon ions as local ablative treatment in patients with primary liver cancer. Radiat Oncol 2025;20:23. https://doi.org/10.1186/s13014-025-02594-y.
[5] Abousaida B, Seneviratne D, Hoppe BS, Ko SJ, Asaithamby A, Cucinotta FA, et al. Carbon ion radiotherapy in the management of hepatocellular carcinoma. JHC 2021;8:1169–79. https://doi.org/10.2147/JHC.S292516.
[6] Paganetti H. Range uncertainties in proton therapy and the role of Monte Carlo simulations. Phys Med Biol 2012;57:R99–. https://doi.org/10.1088/0031-9155/57/11/R99.
[7] Hoffmann A, Oborn B, Moteabbed M, Yan S, Bortfeld T, Knopf A, et al. MR-guided proton therapy: a review and a preview. Radiat Oncol 2020;15:129. https://doi.org/10.1186/s13014-020-01571-x.
[8] Paganetti H, Botas P, Sharp GC, Winey B. Adaptive proton therapy. Phys Med Biol 2021;66. https://doi.org/10.1088/1361-6560/ac344f.
[9] MacKay RI. Image guidance for proton therapy. Clin Oncol 2018;30:293–8. https://doi.org/10.1016/j.clon.2018.02.004.
[10] Regnery S, Pestana R, Hoffmeister-Wittmann P, Mielke T, Hoegen-Saßmannshausen P, Weykamp F, et al. 1438 Image-guided carbon ion stereotactic radiotherapy of hepatocellular carcinoma: paving the way for MRguided online adaptive therapy. Radiother Oncol 2025;206:S1770–2. https://doi.org/10.1016/S0167-8140(25)00458-X.
[11] Pestana R, Seidensaal K, Beyer C, Debus J, Klüter S, Bauer J. Evaluation of pelvic MRI-to-CT deformable registration for adaptive MR-guided particle therapy. Int J Part Ther 2024;14:100636. https://doi.org/10.1016/j.ijpt.2024.100636.
[12] Padgett KR, Simpson G, Asher D, Portelance L, Bossart E, Dogan N. Assessment of online adaptive MR-guided stereotactic body radiotherapy of liver cancers. Phys Med 2020;77:54–63. https://doi.org/10.1016/j.ejmp.2020.07.027.
[13] Feng M, Suresh K, Schipper MJ, Bazzi L, Ben-Josef E, Matuszak MM, et al. individualized adaptive stereotactic body radiotherapy for liver tumors in patients at high risk for liver damage: a phase 2 clinical trial. JAMA Oncol 2018;4:40–7. https://doi.org/10.1001/jamaoncol.2017.2303.
[14] Stanescu T, Shessel A, Carpino-Rocca C, Taylor E, Semeniuk O, Li W, et al. MRI-guided online adaptive stereotactic body radiation therapy of liver and pancreas tumors on an MR-linac system. Cancers 2022;14:716. https://doi.org/10.3390/cancers14030716.
[15] Lei Y, Matkovic LA, Roper J, Wang T, Zhou J, Ghavidel B, et al. Diffeomorphic transformer-based abdomen MRI-CT deformable image registration. Med Phys 2024;51:6176–84. https://doi.org/10.1002/mp.17235.
[16] Moghaddam AB, Runz A, Augusto RF, Echner G, Johnen W, Gabriel R, et al. A dynamic anthropomorphic phantom for end-to-end testing in image- and surface-guided adaptive radiotherapy. Med Phys 2025;52:e70107. https://doi.org/10.1002/mp.70107.
[17] Elter A, Hellwich E, Dorsch S, Schäfer M, Runz A, Klüter S, et al. Development of phantom materials with independently adjustable CT- and MR-contrast at 0.35, 1.5 and 3 T. Phys Med Biol 2021;66:045013. https://doi.org/10.1088/1361-6560/abd4b9.
[18] Weistrand O, Svensson S. The ANACONDA algorithm for deformable image registration in radiotherapy. Med Phys 2015;42:40–53. https://doi.org/10.1118/1.4894702.
[19] Dice LR. Measures of the amount of ecologic association between species. Ecology 1945;26:297–302. https://doi.org/10.2307/1932409.
[20] Chalana V, Kim Y. A methodology for evaluation of boundary detection algorithms on medical images. IEEE Trans Med Imaging 1997;16:642–52. https://doi.org/10.1109/42.640755.

[21] Siddon RL. Fast calculation of the exact radiological path for a three-dimensional CT array. Med Phys 1985;12:252–5. https://doi.org/10.1118/1.595715.
[22] Taasti VT, Bäumer C, Dahlgren CV, Deisher AJ, Ellerbrock M, Free J, et al. Inter-centre variability of CT-based stopping-power prediction in particle therapy: Survey-based evaluation. Phys Imaging Radiat Oncol 2018;6:25–30. https://doi.org/10.1016/j.phro.2018.04.006.
[23] Longarino FK, Maguire U, Beyer C, Pestana R, Regnery S, Debus J, et al. Stability of liver position in a shuttle-based workflow for daily online magnetic resonance imaging-guided particle therapy. phiRO 2025;35:100795. https://doi.org/10.1016/j.phro.2025.100795.